



Impact of heat storage on remote-sensing based quantification of anthropogenic heat in urban environments

Zhou Yu^a, Leiqiu Hu^b, Ting Sun^c, John Albertson^a, Qi Li^{a,*}

^a School of Civil and Environmental Engineering, Cornell University, Ithaca, NY, United States

^b Department of Atmospheric and Earth Science, University of Alabama in Huntsville, Huntsville, AL, United States

^c Department of Meteorology, University of Reading, Reading, United Kingdom

ARTICLE INFO

Editor: Marie Weiss

Keywords:

Anthropogenic heat flux
Surface energy balance
Heat storage

ABSTRACT

Anthropogenic heat (AH) significantly impacts urban climates. Although combining the surface energy balance (SEB) with remote sensing data (RS-SEB) is promising for AH quantification, it has been shown to yield paradoxical low AH values in urban centers. Some speculation on the causes for the underestimation has appeared in the literature; however, none has been verified or thoroughly evaluated, largely hindering the further improvement of spatial representation of AH estimated through the RS-SEB approach. Here by casting the difference in the SEB between the observed reference state and a hypothetical scenario without AH, we developed a thermal stability analysis framework to identify the primary causes. Using AH estimations from six representative US cities based on Local Climate Zone (LCZ), we find that the reduced efficiency of the pathway from AH to sensible heat flux near high-rise buildings results in greater heat storage, which is a primary contributor to the underestimation. This study highlights the importance of heat storage in AH quantification using remote sensing data and provides evidence for potentially correcting the bias in AH with improved heat storage modeling.

1. Introduction

More than 55% of the global population lives in urbanized areas, but account for nearly 70% of the world's annual energy use (Quah and Roth, 2012). The energy consumed to sustain anthropogenic activities (e.g. transportation, building energy and industrial processes) and human metabolism have been well recognized as an important source term in the energy budget for an urban system across multiple spatial scales (Pigeon et al., 2007; Sailor and Lu, 2004; Allen et al., 2011), often denoted as the anthropogenic heat (AH). As an important component of the urban surface energy balance (SEB), AH impacts the urban climates non-trivially. For example, AH is an important contributor to the urban heat island effect (Bohnenstengel et al., 2014; Chow et al., 2014). The occurrence and spatial distribution of urban precipitation are also sensitive to AH (Holst et al., 2016; Feng et al., 2012; Nie et al., 2017; Zhang et al., 2018). However, accurate description of spatial and temporal evolution of AH is still challenging.

Inventory-based approaches (e.g. (Iamarino et al., 2012; Quah and Roth, 2012; Sailor, 2011; Allen et al., 2011)) derived from energy-consumption data have been successfully applied to quantify AH, often offering temporal profiles of AH but lacking fine-grained spatial

details due to data availability (Dong et al., 2017). The observational-based approach (e.g. (Offerle et al., 2005; Pigeon et al., 2007; Chow et al., 2014)) quantifies AH as a residual term in the SEB, which is usually adopted in the urban meteorology community, when other components of the SEB are directly available from observations such as using flux-tower measurements. However, the term representing change in heat storage in the SEB that can vary with different seasons is often neglected (e.g. (Chow et al., 2014)) and only neighborhood-scale AH can be obtained using this method (i.e. integrated over flux footprint of tower sensors).

On the other hand, much finer spatial detail and wider geographical coverage have been achieved by using remote-sensing based approaches, in which different methods have been developed for mapping AH estimates for a diverse range of spatial-temporal scales (e.g. (Zhang et al., 2019; Chrysoulakis et al., 2018; Kato and Yamaguchi, 2005)). One of the widely adopted methods considers the urban SEB and uses the easily accessible remotely sensed (RS) surface temperatures from satellite platforms to quantify AH (Kato and Yamaguchi, 2005) hereafter referred as the RS-SEB method. First developed by Kato and Yamaguchi (2005), the RS-SEB method is based on the idea that AH-induced increases in air and surface temperatures predominantly raise the sensible

* Corresponding author.

E-mail address: ql56@cornell.edu (Q. Li).

heat flux, with only negligible effects on other terms in the SEB. In essence this is to assume that all of the AH is removed from the control volume by the sensible heat pathway. Later applications of the RS-SEB method have unequivocally adopted this assumption (Zhou et al., 2012; Wong et al., 2015). Despite reasonable spatial distribution of AH at the regional-scale, finer grained studies have resulted in anomalously low values of AH in parts of the urban center (Kato and Yamaguchi, 2005; Wong et al., 2015; Zhou et al., 2012), contradicting both common sense and inventory-based data (Zhou et al., 2012; Dong et al., 2017). This phenomenon has been speculated to be caused by the shading of tall buildings causing deviations in skin temperature, e.g., in Kato and Yamaguchi (2005), but no clear consensus has been reached. Therefore, we explore here in greater depth the underlying key assumption of the RS-SEB for AH quantification.

If we consider a typical control volume containing the top of the roughness sublayer to the depth in the ground with zero diurnally averaged conductive heat flux, the urban SEB with the effect of anthropogenic heating is given by

$$R_n + AH = H + LE + \Delta S, \quad (1)$$

where R_n , ΔS , H and LE are the net all-wave radiation, net rate of change in heat storage (hereafter as heat storage for brevity), and turbulent sensible and latent heat fluxes, respectively. In particular, depending on the way in which anthropogenic energy sources are distributed in the control volume (i.e., building energy use, traffic heat exhausts and human metabolism, etc.), AH may cause a non-negligible change in ΔS , which is the net energy stored (or released) by all substances in the control volume (e.g. the canopy air, buildings, ground, vegetation and human beings, etc.) (Oke et al., 2017). It can be conjectured that the transient effect of AH on ΔS may lead to violation of the assumption of AH being directly converted to H in the RS-SEB method. Nevertheless, few studies thus far have targeted the resolution of this issue. Furthermore, the relative impacts of different urban land use and land cover (LULC) types on this assumption remain relatively understudied, which hampers our understanding of the reliability of the RS-SEB method at the neighborhood scale within a city.

Motivated by the aforementioned knowledge gaps, this paper first examines the variation of AH estimates across different urban LULC types classified according to the local climate zones (LCZs) (Stewart and Oke, 2012) in Section 2. Then, in Section 3 we present a new theoretical analysis framework to examine the impact of heat storage on the RS-SEB method. Final remarks and conclusions are presented in Section 4.

2. AH estimation from satellite observations using the RS-SEB method

To examine the profile of AH estimates across LCZ types for a range of cities, we first estimate AH with the classic RS-SEB method (Kato and Yamaguchi, 2005) for six cities in the US with contrasting sizes and background climates (Chicago, Washington DC, Houston, Los Angeles, Philadelphia, and Phoenix). One scene of Landsat 8 imagery under clear-sky was selected for each city. The collected images mainly fall in spring and fall months, since background climates in different cities mostly affect energy use for heating and cooling in winter and summer (Sailor, 2011), we minimized the impacts of such difference and only focus on the ‘baseline’ anthropogenic heat in spring and fall. However, in some cities energy use for heating and cooling may still impact the magnitudes of anthropogenic heat flux in the two selected seasons. Therefore, instead of focusing on the magnitudes, the variability of anthropogenic heat flux across different LCZ types will be examined (see next paragraph). The components of the SEB were computed following similar procedures and methods as outlined in Kato and Yamaguchi (2005), with details of the computation presented in Appendix A.

The urban LULC types were classified according to the LCZs, which Stewart and Oke (2012) defined to be ‘regions of uniform surface cover,

structure, material, and human activity that span hundreds of meters to several kilometers in horizontal scale’. The LCZ classification maps were obtained from the World Urban Database and Access Portal Tools (WUDAPT) (Ching et al., 2018), where LCZ types 1 to 10 (See Figs. 1b and d) denote compact high-rise (LCZ 1), compact mid-rise (LCZ 2), compact low-rise (LCZ 3), open high-rise (LCZ 4), open mid-rise (LCZ 5), open low-rise (LCZ 6), light-weight low-rise (LCZ 7), large low-rise (LCZ 8), sparsely built (LCZ 9) and heavy industry (LCZ 10), respectively. The urban canopy parameters needed for the computation were obtained from level-zero data products provided by WUDAPT. In general, AH in a city computed from a single satellite scene is not representative of the annual average. However, in the default level-zero database of AH from the WUDAPT (here defined as $AH_i^{default}$ for the i^{th} LCZ), $AH_i^{default}$ is the annual average value of AH adopted from the criteria for LCZ classification (Stewart and Oke, 2012, Table 4). In fact, AH varies significantly with season, location, and level of energy consumption of an individual city (Stewart and Oke, 2012). To remove these confounding issues from the comparison, we focus on how AH^{RS-SEB} varies across LCZ within any given city. To increase the statistical power of the comparison, we compute AH^{RS-SEB} for each LCZ by averaging across all of the satellite image pixels corresponding to that LCZ type in a city. Therefore, the profile of AH^{RS-SEB} across LCZs would represent the persistent structural differences in energy use intensity across different LCZs. Here, instead of comparing the magnitudes of AH_i^{RS-SEB} derived from a single scene with $AH_i^{default}$ that reflects an annual average, we focus on interrogating their respective variations across the LCZs to reveal any similarity or contrast.

Before interrogating the LCZ dependence of AH, we look at the spatial distribution of the estimated AH using the RS-SEB method and the corresponding LCZ maps for Chicago and Philadelphia in Fig. 1, as two examples. We note oddly low values of AH can be clearly identified in regions classified as compact high-rise (LCZ 1) and open high-rise (LCZ 4) in the downtown areas. These patterns consistently occur in other selected cities and are in stark contrast to the spatial distributions of AH estimated using inventory-based approach (Chow et al., 2014; Pigeon et al., 2007; Roberts et al., 2006). The RS-SEB based AH estimates for all cities were averaged by LCZ type (AH_i^{RS-SEB}) and are presented alongside the inventory estimates of $AH_i^{default}$ in Table 2. The magnitudes of AH_i^{RS-SEB} vary significantly across the cities, as expected to reflect the city-specific AH characteristics. Our interest here is in variability of AH across LCZ type for a given city, and the extent to which the shape of such an AH-LCZ profile is consistent across different cities. The high-rise LCZ’s show lower AH values ($AH_1^{default}$, $AH_4^{default}$) than the low-rise LCZ’s ($AH_3^{default}$, $AH_6^{default}$) across the range of cities, as apparent in the puzzling spatial pattern noted in Fig. 1. It is common to have actual AH values up to several hundreds of $W \cdot m^{-2}$, especially in central urban areas during daily peak hours (Wong et al., 2015; Zhou et al., 2012). We also note that magnitudes of AH_i^{RS-SEB} in some LCZs such as LCZ 8 (large low-rise) and LCZ 9 (sparsely built) in Table 1 are large. This is likely related to the heat storage change (ΔS) being modeled as $C_g R_n$ (See Appendix A.2), where the traditional fraction taken from the literature of $C_g=0.7$ has recently been questioned as being too large (e.g. (Oke et al., 2017, Fig. 6.12)). However, instead of focusing on tuning ΔS in the RS-SEB method, we re-examine the underlying assumption of this method and thus use the same value of C_g as that in Kato and Yamaguchi (2005) for consistency.

Fig. 2 shows the LCZ dependence of AH_i^{RS-SEB} normalized by the respective city averaged values at the observation time (AH_{mean}^{RS-SEB}) (solid markers, left y-axis). $AH_i^{default}$ is normalized by $AH_{mean}^{default}$, which is the default AH weighted by the area fractions of LCZs in each city and averaged across all studied cities, $\overline{AH_i^{default}} / \overline{AH_{mean}^{default}}$ (open circles, right y-axis). Here, we are particularly interested in LCZ 1–6 as they represent two categories of urban construction density: compact (LCZ 1, 2 and 3) and open (LCZ 4, 5 and 6), where the mean building height decreases with increasing LCZ number within each category (i.e. 1 to 3, and 4 to 6). Across the studied cities, the magnitudes of $AH_i^{RS-SEB} / AH_{mean}^{RS-SEB}$

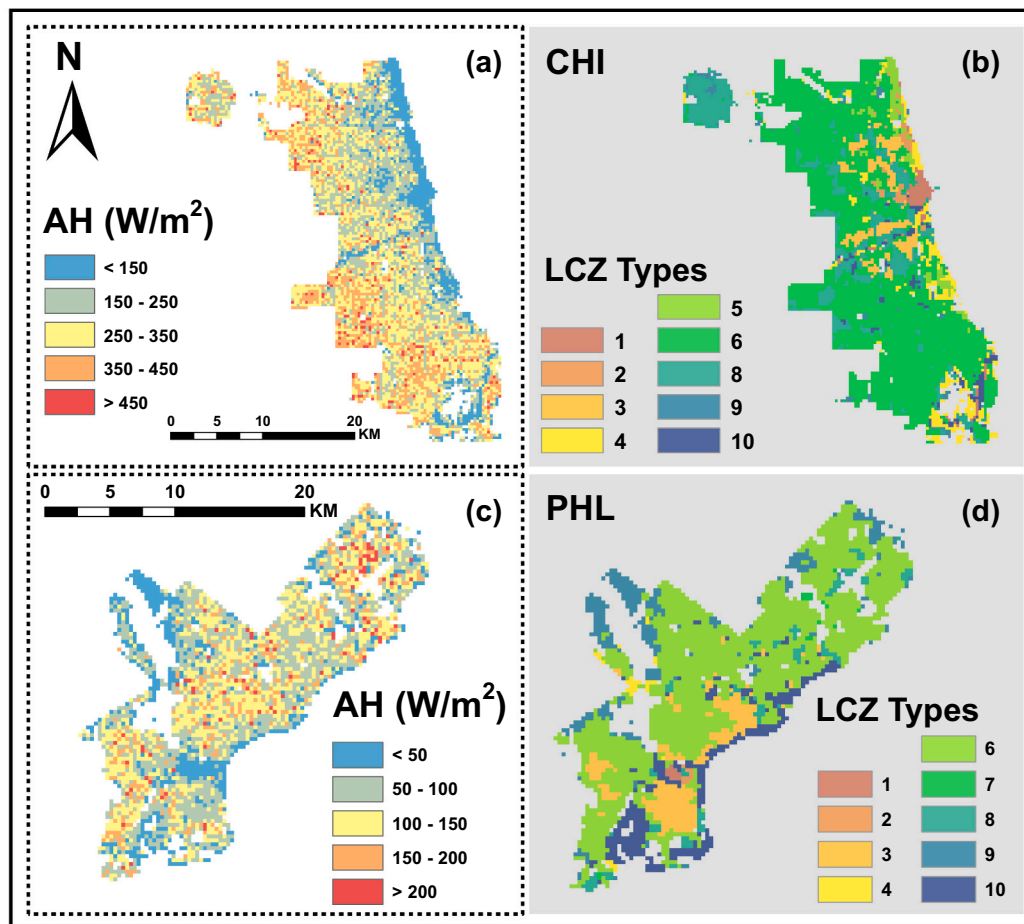


Fig. 1. Two examples of the selected cities (Chicago, 20,170,915, 16:35 UTC and Philadelphia, 20,171,002, 15:40 UTC) AH results (a, c) and LCZ classifications (b, d) (1: compact high-rise; 2: compact mid-rise; 3: compact low-rise; 4: open high-rise; 5: open mid-rise; 6: open low-rise; 7:light-weight low-rise; 8: large low-rise; 9: sparsely built; 10: heavy industry).

Table 1
 AH^{RS-SEB} across LCZs in different cities and $AH^{default}$ (WUDAPT) (unit: W/m^2).

	CHI	DC	HOU	LA	PHL	PHX	WUDAPT
LCZ 1	28.82	81.01	24.64	185.53	-36.87	182.02	175
LCZ 2	111.00	132.30	102.69	/	24.83	/	37.5
LCZ 3	272.49	176.39	/	380.82	104.72	376.24	37.5
LCZ 4	131.58	/	39.26	/	2.41	211.43	25
LCZ 5	94.17	104.85	92.36	278.93	/	282.03	12.5
LCZ 6	297.47	114.69	161.17	345.50	107.52	389.06	12.5
LCZ 7	/	/	/	460.85	91.64	364.16	17.5
LCZ 8	271.18	173.45	139.11	370.48	123.45	362.19	25
LCZ 9	267.50	27.58	55.12	300.33	45.59	357.79	5
LCZ 10	220.79	/	53.57	307.07	52.20	310.41	350

Note: CHI – Chicago (20,170,915, 16:35 UTC); DC – District of Columbia (20,170,923, 15:46 UTC); HOU – Houston (20,170,406, 16:50 UTC); LA – Los Angeles (20,171,015, 18:28 UTC); PHL – Philadelphia (20,171,002, 15:40 UTC); PHX – Phoenix (20,171,003, 18:04 UTC).

generally increase with decreasing building height in each category, in stark contrast to the decrease of $AH_t^{default} / AH_{mean}^{default}$ (solid circles). These results are consistent with previous findings that low values of AH occur in parts of the urban center (where taller buildings are likely to be found) (Wong et al., 2015; Zhou et al., 2012; Kato and Yamaguchi, 2005). These RS-SEB results run counter to the tendency for taller buildings to imply more energy consumption per unit ground area, as seen in the inventory data. Here we further demonstrate that the RS-SEB method leads to low AH values in both dense and open urban construction density, which suggests a cause beyond the proposed shading effect of buildings (Kato and Yamaguchi, 2005). Now, in the following

section, we proceed to more deeply examine our conjecture about the role played by the net change in heat storage.

3. The impact of AH on heat storage in the SEB

To understand the reason for the systematic low values of AH in LCZs characterized by high-rise buildings, we re-examine the underlying assumption of the RS-SEB method – that AH completely causes an increase in sensible heat flux. When integrated over time scales far exceeding one day, ΔS , the net rate of change in heat storage becomes much smaller than other terms in the SEB, and the underlying

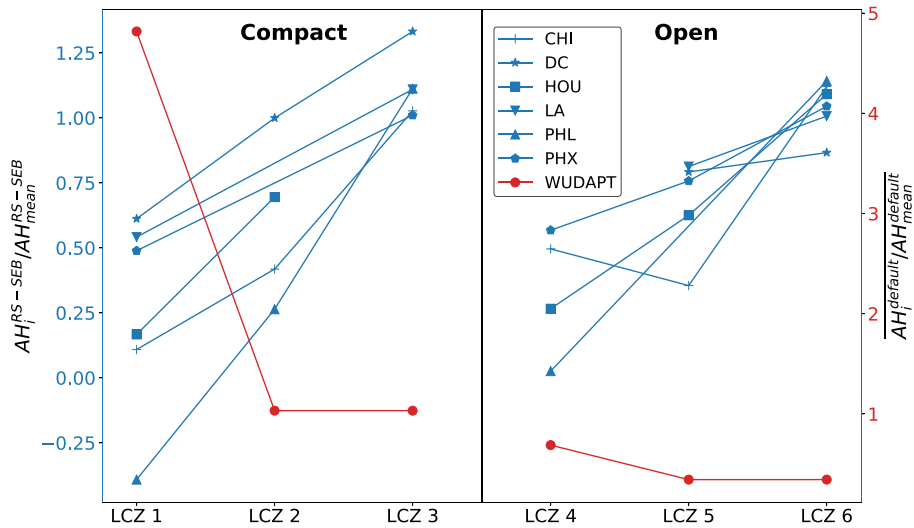


Fig. 2. Variation of $\frac{AH_i^{RS-SEB}}{AH_{mean}^{RS-SEB}}$ (Blue lines and left Y axis) and $\frac{AH_i^{default}}{AH_{mean}^{default}}$ (red lines and right Y Axis) across different LCZs. LCZs 1–3 (LCZs 4–6) are characterized by compact (dense) urban density with descending mean building height (i.e., decreasing volume of built materials per unit area from LCZ 1 (LCZ 4) to LCZ 3 (LCZ 6)). (For interpretation of the references to colour in this figure legend, the reader is referred to the web version of this article.)

assumption becomes reasonable. However, on sub-daily time scales, especially for a snapshot in time as with remote sensing, the partitioning of instantaneous AH into other components in the SEB may be significant (Hanna et al., 2011; Roberts et al., 2006). Here we consider two scenarios: the first scenario (Case No-Humans) represents a generic urban surface without any human energy use (e.g., metabolism, indoor energy use, transportation, industry, etc.); the second scenario (Case With-Humans) is the same as Case No-Humans, except for the presence of human activities (i.e., anthropogenic energy sources). Components of the SEB in Case With-Humans thus differ from those in Case No-Humans only due to the effects of AH. The SEB for Case With-Humans applied to the three-dimensional control volume indicated in Fig. 3a can be written as

$$R_n + R_{na} + AH = \Delta S + \Delta S_a + LE + LE_a + H + H_a, \quad (2)$$

and the corresponding SEB for Case No-Humans is $R_n = \Delta S + LE + H$, where the subscript ‘a’ denotes the anthropogenically-induced perturbation to each base component. The effect of advection on the SEB is neglected. Although the anthropogenic latent heat flux can also be significant in urban areas especially from cooling systems in summer (Sailor, 2011; Moriwaki et al., 2008), for the selected data in spring and fall, the direct anthropogenic emission of water vapor is not considered.

However, the potential thermally-induced change to LE from AH is still considered via LE_a . The difference in SEB between these two scenarios is $AH = \Delta S_a + LE_a + H_a - R_{na}$. (3)

The commonly adopted assumption after Kato and Yamaguchi (2005) is $AH \approx H_a$, with R_{na} , ΔS_a , and LE_a assumed to be negligible. If the turbulent fluxes are measured, such as by using eddy-covariance measurements, then AH can be unequivocally computed from Eq. 2, as the control volume contains all sources of anthropogenic heat emissions, provided $\Delta S + \Delta S_a$ can be accurately determined, which is a known conundrum in urban SEB studies (Roberts et al., 2006). However, viewing from the satellite’s perspective in Fig. 3a, the remotely sensed skin temperature T_s is used to model the SEB components for a two-dimensional surface projection (See Fig. 3b), in which T_s encodes critical information about the partitioning of total available energy from both natural and anthropogenic sources among respective components (Wang et al., 2011; Yang and Wang, 2014). In other words, the anthropogenic heat sources in the three-dimensional control volume act to alter the skin temperature T_s with modulation by the heat transfer processes (i.e. radiation, convection and conduction), which critically depend on the specific details of how the anthropogenic heat sources are distributed.

From the perspective of energy dissipation in the surface energy

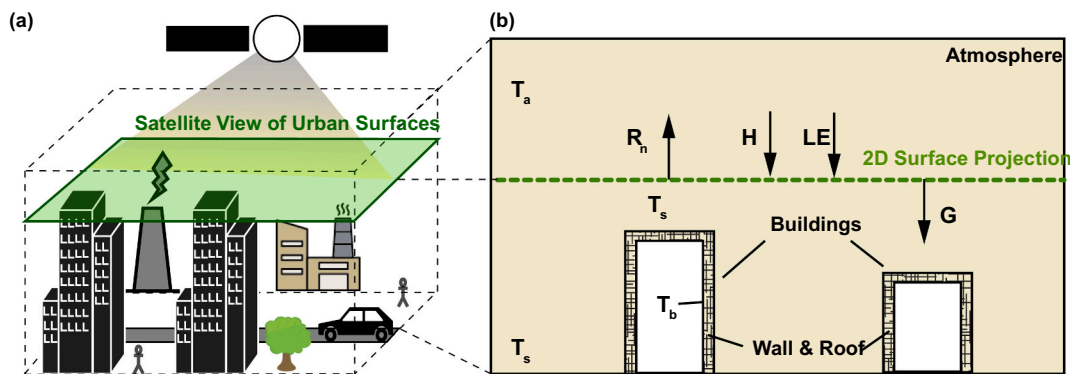


Fig. 3. (a) Schematics of a three-dimensional control volume and a two-dimensional surface projection viewed from the satellite. (b) Surface energy budget in the two-dimensional projected surface, which does not explicitly contain sources of anthropogenic heat emissions. However, the three temperatures components (the skin temperature T_s , the inner building wall temperature T_b and the air temperature T_a) are already modified by sources of anthropogenic heat emissions. T_s retrieved from the satellite represents an effective surface temperature from all surfaces including the ground and roofs.

budget (Bateni and Entekhabi, 2012) for a generic surface, the total available energy is dissipated via sensible, latent, ground heat fluxes and outgoing longwave radiation. Partitioning of total available energy depends on the relative efficiencies of dissipation via these pathways (Bateni and Entekhabi, 2012; Sun et al., 2013). Insight into the partitioning of AH can be gained by applying the force-store approach (Garratt, 1994) to the skin temperature T_s for urban surfaces (Swaaid, 1995; Oke et al., 1991; Johnson et al., 1991; Miao et al., 2006) (Fig. 3b), followed by a stability analysis of the SEB (Bateni and Entekhabi, 2012). The procedures are outlined briefly here and details of the derivation are presented in Appendices B and C.

First, for a generic urban surface without influence by anthropogenic heating (Fig. 3b), the change in heat storage ΔS (c.f. Eq. 1) is equal to the conductive heat flux at the material surface (Sun et al., 2017), G , where G is constrained by the surface energy balance given by $G = R_n - H - LE$. We assume that for this material surface under consideration, the net effect of human activities (i.e. anthropogenic heating) manifests itself by perturbing the thermal boundary conditions of the conductive heat transfer process. Specifically, the building interior wall temperature T_b (Johnson et al., 1991; Oke et al., 1991) and the air temperature T_a are altered, where the deviations are denoted as δT_a and δT_b . T_s is subsequently altered and the change is denoted as δT_s . The increase of air temperature by AH is due to direct heat discharge from traffic and industry processes. Assuming that in the selected spring and fall seasons, there is no indoor cooling by air conditioning, the increase in the interior wall temperature is then solely due to lighting, electrical appliances and other human activities. The perturbed temperatures for this material surface then lead to modified surface energy balance, thus the change in G due to anthropogenic heating can be denoted as $\delta G = \delta R_n - \delta H - \delta LE$.

Then, the temporal evolution of the material surface temperature T_s can be studied using the force-restore approach, which has been applied in the urban context (Johnson et al., 1991; Oke et al., 1991), where the restoring temperature is the interior building wall temperature T_b . The new development here is to extend the force-restore approach to a stability analysis framework (Bateni and Entekhabi, 2012), which reveals the difference in temporal evolution of T_s between the cases of No-Humans and With-Humans. The rate of change of T_s is given by an ordinary differential equation for Case No-Humans:

$$\frac{dT_s}{dt} = \frac{\omega^{1/2}}{P} G(t) - \omega(T_s - T_b); \quad (4)$$

and for Case With-Humans:

$$\frac{d(T_s + \delta T_s)}{dt} = \frac{\omega^{1/2}}{P} (G(t) + \delta G(t)) - \omega(T_s + \delta T_s - (T_b + \delta T_b)), \quad (5)$$

where ω is the principal diurnal frequency corresponding to the principal Earth rotation frequency: $\frac{1}{24 \times 3600} \text{ s}^{-1}$; P is the thermal inertia of the surface material with units $\text{J} \cdot \text{m}^{-2} \cdot \text{K}^{-1} \cdot \text{s}^{-1/2}$, calculated from WUDAPT database. The time evolution of δT_s , the resultant change in T_s due to perturbation by AH, is given by Eq. 5 - Eq. 4 as:

$$\frac{d\delta T_s}{dt} = \frac{\omega^{1/2}}{P} (\delta G) - \omega(\delta T_s - \delta T_b), \quad (6)$$

where δG , the change to G caused by anthropogenic heat emissions, can be substituted using the relation $\delta G = \delta R_n - \delta H - \delta LE$. Since the net short wave radiation is not impacted by δT_s and δT_a , δR_n is given by the change in longwave radiation (LW) (i.e., $\delta R_n = \delta LW$), Eq. 6 becomes

$$\frac{d\delta T_s}{dt} = \frac{\omega^{1/2}}{P} (\delta LW - \delta H - \delta LE) - \omega(\delta T_s - \delta T_b) \quad (7)$$

Applying the bulk parameterizations for sensible and latent heat fluxes and a linearization of the Stefan-Boltzmann relation for the longwave radiation, Eq. 7 becomes

$$\frac{d\delta T_s}{dt} = - \left(1 + \frac{r_a}{r_o} + \beta \frac{\delta}{\gamma} + \frac{r_a}{r_g} \right) \delta T_s + Q', \quad (8)$$

where τ is t normalized by $Pr_a / \sqrt{\omega} \rho c_p$ and the full expressions for $\frac{r_a}{r_o}$, $\beta \frac{\delta}{\gamma}$, $\frac{r_a}{r_g}$ and Q' can be found in Appendix B. The negative coefficient on δT_s reflects the dissipative nature of the system towards the equilibrium state δT_s^* in the long time limit, which is $\delta T_s^* = \frac{Q'}{1 + \frac{r_a}{r_o} + \beta \frac{\delta}{\gamma} + \frac{r_a}{r_g}}$. The right hand side of Eq. 8 indicates that the rate at which the system reaches its long time limit equilibrium is dependent on the four pathways, with the relative efficiencies of outgoing longwave radiation, latent heat flux and net rate change of heat storage at the surface relative to sensible heat flux given by $\frac{r_a}{r_o}$, $\beta \frac{\delta}{\gamma}$ and $\frac{r_a}{r_g}$, respectively. For example, $\frac{r_a}{r_g}$ denotes the relative efficiency of G to H in dissipating energy, where r_a is the aerodynamic resistance and r_g is the surface conductive heat flux resistance given by:

$$r_g = \frac{\rho C_p}{P \sqrt{\omega}} \quad (9)$$

It is worth noting that Oke et al. (2017, in Eq. 6.4) defines the ratio between thermal inertia of the urban surface materials, $\mu_g = P / \sqrt{2}$, and that of the air, μ_a , which indicates the sensible heat sharing between the urban surface materials and the turbulent air. However, here $\frac{r_a}{r_g}$ signifies the relative importance of heat storage change compared to sensible heat flux in contributing to the observed T_s given the net available energy from both radiation and anthropogenic heating. For the usual assumption underlying the RS-SEB method to be valid, the term $\frac{r_a}{r_g}$ should be much smaller than one. A large value of $\frac{r_a}{r_g}$ indicates that AH results in non-negligible change in the net rate change of heat storage, invalidating this assumption. Thus, we examine $\frac{r_a}{r_g}$ across LCZ types 1–6 (Fig. 4). Fig. 4a compares $\frac{r_a}{r_g}$ and gridded AH normalized by the difference between maximum and minimum values in each city (Chicago and Philadelphia as examples are shown in Fig. 4a). Relatively high values of $\frac{r_a}{r_g}$ are found in areas with a relatively low amplitude of AH, which usually overlap with the high-rise LCZ types. An ensemble average of the LCZ-specific values of $\frac{r_a}{r_g}$ and AH_i^{RS-SEB} across the sample of cities is considered (Fig. 4b), where for LCZ type $i = 1 - 6$ they are denoted as $\overline{\frac{r_a}{r_{gi}}}$ and $\overline{AH_i^{RS-SEB}}$. Fig. 4b indicates distinctly opposite trends across the LCZs. Details of $\frac{r_a}{r_{gi}}$ are further illustrated in Table 2 for each selected city. Generally, for a given degree of urban surface compactness summarized by the LCZ types (e.g., compact high, medium and low-rise buildings in LCZs 1–3, respectively), $\frac{r_a}{r_g}$ decreases with decreasing building height, in contrast to variation of AH across the LCZ types. The intra-city differences are mainly due to thermal inertia P (e.g. Values of P in LCZ 4–6 are 1.04×10^3 , 0.98×10^3 and $0.89 \times 10^3 \text{ J} \cdot \text{m}^{-2} \cdot \text{K}^{-1} \cdot \text{s}^{-1/2}$, respectively), while the inter-city differences can be attributed to different aerodynamic resistance r_a . For example, r_a in Chicago ranges from 20 to 30 $\text{s} \cdot \text{m}^{-1}$ in the selected day; while in Houston, r_a ranges from 60 to 70 $\text{s} \cdot \text{m}^{-1}$. These results indicate that for urban surfaces characterized by high and dense building fractions, heat storage is a significant pathway for anthropogenic heat. Therefore, the key assumption that $AH \approx H_a$ in the RS-SEB method is not applicable in urban land surfaces where the anthropogenic energy source is more effectively partitioned into G . A simple parameterization for G as a fraction of R_n will not account for the partitioned AH, and therefore can lead to consistent underestimation of AH.

4. Conclusion

Remote sensing is an important emerging technique in AH quantification and estimation of urban surface energy fluxes (Chrysoulakis et al., 2018). The effects of AH intertwined with other components of the SEB impose significant challenges to quantify

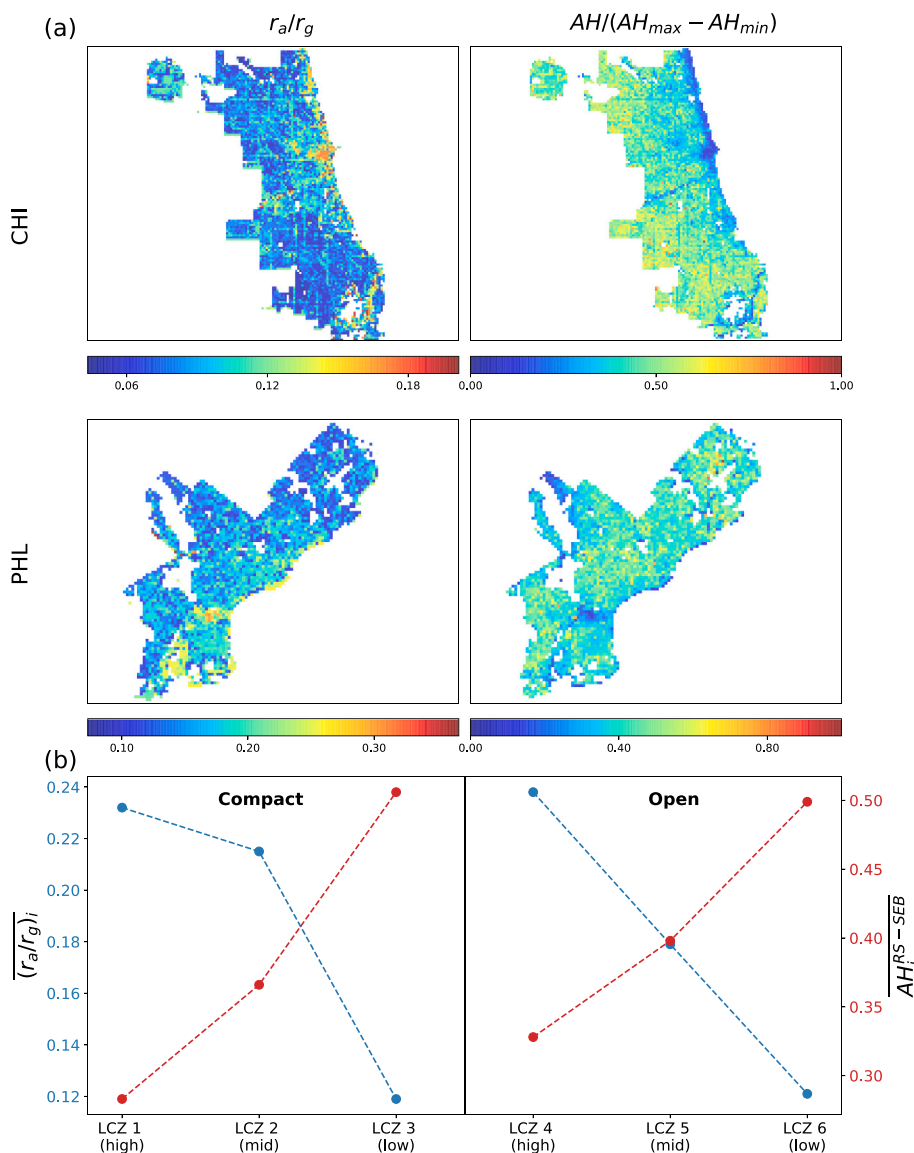


Fig. 4. (a) Left column: Energy partitioning efficiencies of heat storage relative to the sensible heat flux in Chicago (CHI) and Philadelphia (PHL). Right column: pixel-wise AH normalized with the difference between maximum AH and minimum AH in respective cities. (b) $\overline{(r_a/r_g)_i}$ and $\overline{AH_i^{RS-SEB}}$ for LCZ type i , where $i=1,2,3,4,5,6$, averaged over the ensemble of cities.

Table 2
Means of r_a/r_g in selected LCZs.

	LCZ 1	LCZ 2	LCZ 3	LCZ 4	LCZ 5	LCZ 6
CHI	0.146	0.133	0.084	0.121	0.113	0.078
DC	0.158	0.147	0.091	/	0.128	0.089
HOU	0.369	0.351	/	0.383	0.323	0.184
LA	0.223	/	0.129	/	0.164	0.110
PHL	0.280	0.229	0.174	0.232	/	0.150
PHX	0.214	/	0.118	0.217	0.165	0.114

changes in the SEB due to anthropogenic energy emissions (i.e., the urban function) (Oke et al., 2017). The non-negligible change of heat storage term in the SEB caused by addition of AH becomes important on sub-daily time scales, which critically impact the quality and reliability of AH estimated by the RS-SEB method. The implication of AH-induced change in heat storage is accessed in this study using satellite observations of the land surface temperature combined with analytical investigation under the LCZ classification framework.

Leveraging level-zero data from the WUDAPT, we estimated LCZ-type-specific AH in six US cities from Landsat 8. The resultant maps of AH and the corresponding statistics indicate that LCZs with high-rise buildings (i.e., LCZ 1 and 4) are more inclined to have lower values of AH than those characterized by low-rise buildings (i.e., LCZ 3 and 6), regardless of the built-up density, which is opposite to the patterns found in WUDAPT reference values adopted from the LCZ classification criterion (Stewart and Oke, 2012). The discrepancy highlights the importance of AH-induced change in heat storage, especially in LCZs with high volume of built materials per unit area. Thus, the assumption of the RS-SEB method, which proposes AH does not alter other components of the SEB except for the sensible heat flux (Kato and Yamaguchi, 2005), can be violated in these LCZs. This implies that on sub-diurnal time scales, the high thermal inertia of building materials causes high heat storage, thus the time lag between building energy consumption and surface temperature increment that is detectable by the remote sensing instruments can significantly deteriorate the reliability of AH computed from the RS-SEB method. It is also noteworthy that the inventory-based method can be affected by this phenomena, since the

time lag between energy consumption and conversion to anthropogenic sensible heat flux is neglected (Sailor, 2011), introducing uncertainty in deriving the sub-diurnal temporal profile of AH. Subsequent stability analysis of the SEB equation indicates that the efficiency of energy partitioning between sensible heat and heat storage given by the ratio of the resistance factors ($\frac{r_a}{r_g}$) is critical in identifying areas prone to errors in AH using the RS-SEB method.

In light of the emergence of databases for urban LULC representations (e.g., the WUDAPT (Ching et al., 2018)) and the promising results of using satellite observations to quantify urban surface fluxes (Chrysoulakis et al., 2018), there is a great potential for integrating earth observations into quantification of AH with a unified platform of urban LULC database. With relatively straightforward data acquisition, the RS-SEB method can potentially be extended to cities worldwide and coupled with numerical weather and climate models for city-specific AH profiles. However, the significant impact of AH on heat storage is a key determining factor for its applicability, especially in urban core areas (e.g. LCZ 1 and LCZ 4) with high ratio of $\frac{r_a}{r_g}$. It is recommended that for neighborhoods with a high ratio of $\frac{r_a}{r_g}$, alternative methods to estimate AH such as the inventory method may complement the RS-SEB method. Although overcoming the deficiency of this method is beyond the scope of this study, future research on remote-sensing-based quantification of AH will benefit from improving the representation of the heat storage term (Lindberg et al., 2020; Hrisko et al., 2021) when applying the RS-SEB method. In addition, it implies that AH-induced change in other components of the urban SEB should be cautiously assessed, especially the time-lag between AH and sensible heat for evaluating the impact of AH on time-dependent urban climate phenomena such as precipitation (Holst et al., 2016; Feng et al., 2012; Nie et al., 2017; Zhang et al., 2018).

Appendix A. AH quantification using the RS-SEB method

First, all data from external sources are listed here:

Satellite products: Landsat 8 level 1 and level 2 (surface reflectance) images at Chicago (20170915), District of Columbia (20170923), Houston (20170406), Los Angeles (20171015), Philadelphia (20171002) and Phoenix (20171003).

Meteorological observations: wind speed and air temperature from ASOS 1-min data corresponding to the time of satellite passing. The observation site is the local airport at each city.

Atmospheric correction parameters (atmospheric transmission, effective bandpass upwelling radiance and effective bandpass downwelling radiance) required in the retrieval of land surface temperature are calculated by a tool from NASA (atmcorr.gsfc.nasa.gov/), using the mid-latitude summer mode.

LCZ-specific urban canopy parameters (e.g. zero-plane displacement height, plan area density, etc.) are from the level 0 data provided by the World Urban Database and Access Portal Tools (WUDAPT).

We adopt the framework of Kato and Yamaguchi (2005) to estimate AH, which is briefly outlined here. First, sensible heat flux due to radiant heat balance is denoted as H_n , which can be calculated as the residual of the SEB equation where R_n the net radiation is the energy input:

$$H_n = R_n - G - LE \quad (\text{A.1})$$

Secondly, both H_n and the increase in sensible heat flux due to AH, which is denoted as H_{as} , contribute to the total sensible heat flux H :

$$H_n + H_{as} = H \quad (\text{A.2})$$

Therefore, $H_{as} = R_n - G - LE - H$, where R_n , G , LE and H can be calculated from parameterizations using remotely-sensed surface temperature. Although H_{as} is not equivalent to AH, under their assumption that the influence of temperature rise (i.e., increase in both air and surface temperatures due to AH) is only non-negligible for sensible heat in this framework, $H_{as} = AH$. Next we outline how each component in the SEB equation is computed. In general, procedures similar to their study are adopted and whenever appropriate, adaptations of the method to urban land use data provided by the WUDAPT will be described.

A.1. Net Radiation (R_n)

$$\begin{aligned} R_n &= R_{L1} - R_{L1} + R_{S1} - R_{S1} \\ &= \varepsilon_a \sigma T_a^4 - [\varepsilon_s \sigma T_s^4 + (1 - \varepsilon_s) R_{L1}] + (1 - \alpha) R_{S1} \\ &= \varepsilon_s \varepsilon_a \sigma T_a^4 - \varepsilon_s \sigma T_s^4 + (1 - \alpha) G_{SC} \cos \theta_d \tau \end{aligned} \quad (\text{A.3})$$

where ε_s is surface emissivity and ε_a is atmospheric emissivity. T_s and T_a stand for surface temperature and air temperature (K). T_a obtained from the

Credit author statement

Zhou Yu: Conceptualization, Formal analysis, Method, Writing-Original draft, review and editing;

Leiqiu Hu: Method, Writing - Review and editing;

Ting Sun: Method, Writing -Review and editing;

John Albertson: Method, Writing -Review and editing;

Qi Li: Conceptualization, Method, Writing - Original draft, review and editing.

Declaration of Competing Interest

The authors declare that they have no known competing financial interests or personal relationships that could have appeared to influence the work reported in this paper.

Acknowledgement

There are no financial conflicts of interests for any author. This work is funded by NASA's Interdisciplinary Research in Earth Science (IDS) program (80NSSC20K1263). All data used in this study are publicly available. Landsat 8 products can be freely ordered through United States Geological Survey (USGS): <https://earthexplorer.usgs.gov/>. 1-min weather station data are provided by the Automated Surface Observing System (ASOS): <ftp://ftp.ncdc.noaa.gov/pub/data/asos-onemin/>. Information regarding local climate zone (LCZ) classification maps and related surface descriptors are available from the World Urban Database and Access Portal Tools (WUDAPT) level 0 database: <http://www.wudapt.org/>.

local airport in each city is assumed to be representative of the entire study area. This simplification is justified because as reported in a study (Crawford et al., 2018) that estimates heat flux from remotely-sensed land surface temperature, unevenly distributed air temperature in cities and non-uniform installation of sensors can introduce uncertainty in spatial interpolation of the air temperature. Furthermore, the spatial variability of air temperature above the urban canopy layer is much less than that of remotely-sensed land surface temperature. Therefore, they opted for using a single reliable air temperature measurement for flux estimation. α is surface albedo, calculated on top of band-wise surface reflectance (Wang et al. 2016). σ is the Stefan-Boltzmann Constant ($5.67 \times 10^{-8} \text{ W} \cdot \text{m}^{-2} \cdot \text{K}^{-4}$). G_{SC} is the Solar Constant: $1360.5 \text{ W} \cdot \text{m}^{-2}$. θ is the zenith angle of observation. d_r is the Earth-Sun distance. θ and d_r are included in the Landsat 8 level 1 product. τ is the air transmissivity provided by the Atmospheric Correction Parameter Calculator of NASA.

A.2. Ground Heat (G)

Ground heat flux can be considered to be proportional to net radiation:

$$G = C_g R_n \quad (\text{A.4})$$

where C_g is the determining coefficient. For urban lands, a universal value of 0.7 is used (Kato and Yamaguchi, 2005).

A.3. Sensible Heat (H)

$$H = \rho C_p \frac{T_s - T_a}{r_a} \quad (\text{A.5})$$

where ρ is air density and C_p is specific heat capacity of air. The land surface temperature T_s , is an alternative of aerodynamic temperature (T_{aero}) for its easier access. r_a refers to aerodynamic resistance.

A pixel-wise modeling of r_a is introduced on three parameters below instead of taking rule-of-thumb values against different land-use types:

- **zero-plane displacement height d .**

This is defined as the mean height of momentum absorption by a tall canopy. It is approximately two thirds of the height of overlying obstacles on natural surfaces. Combining the model from wind-tunnel experiments (Macdonald et al., 1998) and urban morphological data, we specify its calculation on every individual urban pixel as below:

$$\frac{d}{H} = 1 + A^{-\lambda_p} (\lambda_p - 1) \quad (\text{A.6})$$

where H is the mean height of obstacles, replaced by mean building height within a grid. λ_p is the plan area density. A is a simulated constant, which is 4.43 for staggered obstruction arrays under urban settings (Macdonald et al., 1998). The values of H and λ_p are obtained from the level 0 data in WUDAPT and Oke et al. (2017), respectively (Table A.3).

Table A.3

H and λ_p values from WUDAPT.

	LCZ 1	LCZ 2	LCZ 3	LCZ 4	LCZ 5	LCZ 6	LCZ 7	LCZ 8	LCZ 9	LCZ 10
H	37.5	17.5	6.5	37.5	17.5	6.5	3	6.5	6.5	10
λ_p	0.5	0.55	0.55	0.3	0.3	0.3	0.75	0.4	0.15	0.25

A.3.1. Wind speed u_z

Wind speed data are from ASOS and nearby automatic weather stations from Weather Underground (wunderground.com) serve as backups only if data of certain days are missing. Wind speed at each urban pixel is extrapolated from the weather station value using the reference height scaling method (Crawford et al., 2018; Wieringa, 1986), where a neutral stability is assumed in this study. This reference height scaling method shown in equations below first interpolates the measured wind speed U to a reference height z_{ref} to obtain U_{ref} , where z_{ref} is assumed to be 200 m, indicating a level high enough for the logarithmic wind profile to be valid. Then, U_{ref} is interpolated to 1.5 times the height of mean obstacle (building) height H at each urban grid to obtain u_z , such that the bulk aerodynamic method for turbulent fluxes parameterization are subsequently applied uniformly across all urban grids at $1.5H$, which is regarded as near the top of the urban roughness sublayer, where the inertial sublayer with a logarithmic wind profile starts. Although the demarcation of inertial sublayer can vary depending on the underlying surface roughness, $1.5H$ seems to be reasonable in computing the aerodynamic resistance as shown in Crawford et al. (2018).

$$U_{ref} = U_{obs} \frac{\ln\left(\frac{z_{ref}-d_{obs}}{z_{0,obs}}\right)}{\ln\left(\frac{z_{m,obs}-d_{obs}}{z_{0,obs}}\right)} \quad (\text{A.7})$$

$$u_z = U_{ref} \frac{\ln\left(\frac{z_m-d}{z_{0m}}\right)}{\ln\left(\frac{z_{ref}-d_{obs}}{z_{0,obs}}\right)} \quad (\text{A.8})$$

d_{obs} is the displacement height at the observational site; $z_{m, obs}$ and $z_{0, obs}$ are the height of wind (momentum) sensor and the roughness length for momentum at the observational site, respectively. The necessary urban parameters for the above interpolation at local airports can be obtained through Davenport classification of effective terrain roughness (Stewart and Oke, 2012; Davenport et al., 2000) and WUDAPT classification of local climates. Each observational site at the local airport is located in the WUDAPT LCZ classification map, where LCZs 8 and 10 are found as the dominant types for sites. Thus, $H=10$ m, $\lambda_p=0.55$, and the computed displacement height $d_{obs}=8.0$ m. Furthermore, building layouts at each local airport are visually inspected in the Google Map, which then are classified as ‘Rough’ in Davenport classes with $z_{0, obs}=0.25$ m according to the tabulated value.

A.3.2. Roughness length for momentum (z_{0m}) and heat (z_{0h}).

First, the roughness length (z_{0m}) at each pixel is computed following the relation $z_{0m} = 1/10H$ as implemented in Grimmond and Oke (1999). Second, the heat roughness length (z_{0h}) is computed using the kB^{-1} relation (Crawford et al., 2018; Li et al., 2020):

$$\ln \frac{z_{0m}}{z_{0h}} = kB^{-1}, \quad (\text{A.9})$$

in which

$$kB^{-1} = \beta(Re_s)^{0.25} - 2.0,$$

follows the theoretical derivation in (Brutsaert, 1982), where Re_s , the roughness Reynolds number is $\frac{z_{0m}u_*}{\nu}$, u_* being the friction velocity and ν being the kinematic viscosity ($1.46 \times 10^{-5} \text{ m}^2 \text{ s}^{-1}$). The empirical constant β varies according to different surface types (Kanda et al., 2007), here it is modeled with respect to vegetation cover (Crawford et al., 2018), given by $\beta = 0.87e^{-0.997FVC}$, where FVC is the fractional vegetation cover.

The equation for the bulk aerodynamic resistance r_a is:

$$r_a = \frac{\ln\left(\frac{z_m-d}{z_{0m}}\right) \ln\left(\frac{z_m-d}{z_{0h}}\right)}{k^2 u_*}, \quad (\text{A.10})$$

where z_m equals to 1.5 times mean building height, at which height bulk aerodynamic method for turbulent fluxes parameterization applies.

A.4. Latent Heat (LE)

$$LE = \frac{\rho C_p}{\gamma} \frac{e_s - e_a}{r_s + r_a}, \quad (\text{A.11})$$

where γ is the psychrometric constant (approximately $0.66 \text{ hPa} \cdot \text{K}^{-1}$); e_s is saturated water vapor pressure and e_a is actual water vapor pressure (hPa); r_s is the stomatal resistance ($\text{s} \cdot \text{m}^{-1}$). For typical urban area, a reference value of 200 for r_s is used (Zhang et al., 2003).

Appendix B. Stability analysis of the SEB using the force-restore approach

Details of stability analysis of the SEB equation where the force-restore approach is adopted are outlined in this section. In subsequent derivations, the symbol δ indicates the change of some quantity of interest caused by anthropogenic heat.

Change of net longwave radiation is comprised of the change of incoming longwave energy with its outgoing counterpart subtracted:

$$\begin{aligned} \delta LW_{\downarrow} &= \varepsilon_a \sigma (T_a + \delta T_a)^4 - \varepsilon_a \sigma T_a^4 \\ &\approx \varepsilon_a \sigma T_a^4 + 4\varepsilon_a \sigma \delta T_a T_a^3 - \varepsilon_a \sigma T_a^4 \\ &= 4\varepsilon_a \sigma \delta T_a T_a^3 \end{aligned} \quad (\text{B.1})$$

$$\begin{aligned} \delta LW_{\uparrow} &= \varepsilon_s \sigma (T_s + \delta T_s)^4 - \varepsilon_s \sigma T_s^4 + (1 - \varepsilon_s) \delta LW_{\downarrow} \\ &\approx \varepsilon_s \sigma T_s^4 + 4\varepsilon_s \sigma \delta T_s T_s^3 - \varepsilon_s \sigma T_s^4 + (1 - \varepsilon_s) \delta LW_{\downarrow} \\ &= 4\varepsilon_s \sigma \delta T_s T_s^3 + 4(1 - \varepsilon_s) \varepsilon_a \sigma \delta T_a T_a^3 \end{aligned} \quad (\text{B.2})$$

$$\delta LW = \delta LW_{\downarrow} - \delta LW_{\uparrow} = 4\varepsilon_s \varepsilon_a \sigma \delta T_a T_a^3 - 4\varepsilon_s \sigma \delta T_s T_s^3 \quad (\text{B.3})$$

where ε_s and ε_a are surface and air emissivity, respectively; σ is the Stefan-Boltzmann Constant; T_a and T_s are air temperature and surface temperature (K).

Change of δH is attributed to the change of surface temperature and air temperature:

$$\begin{aligned} \delta H &= \rho C_p \frac{(T_s + \delta T_s) - (T_a + \delta T_a)}{r_a} - \rho C_p \frac{T_s - T_a}{r_a} \\ &= \rho C_p \frac{\delta T_s}{r_a} - \rho C_p \frac{\delta T_a}{r_a} \end{aligned} \quad (\text{B.4})$$

where r_a is the aerodynamic resistance ($\text{s}\cdot\text{m}^{-1}$); ρ is the density of air ($\text{g}\cdot\text{m}^{-3}$); C_p is specific heat capacity of air at a constant pressure ($\text{J}\cdot\text{g}^{-1}\cdot\text{K}^{-1}$).

The difference of latent heat is calculated as below, assuming little influence of human activities on actual air humidity (q_a):

$$\begin{aligned} \delta LE &= \frac{\beta\rho L}{r_a}(q_s^*(T_s + \delta T_s) - q_a) - \frac{\beta\rho L}{r_a}(q_s^*(T_s) - q_a) \\ &= \frac{\beta\rho L}{r_a}(q_s^*(T_s + \delta T_s) - q_s^*(T_s)) \\ &\approx \frac{\beta\rho L}{r_a} \left. \frac{\partial q_s^*}{\partial T_s} \right|_{T_s} \delta T_s \end{aligned} \tag{B.5}$$

where β is a parameter related to moisture availability, L is the specific latent heat of vaporization and q_s^*/q_a represents the function for saturated specific humidity/air humidity at given temperature.

Substitute Eq. B.5 and Eq. B.4 in the main text with the above items:

$$\begin{aligned} \frac{d\delta T_s}{dt} &= \frac{\omega^{1/2}}{P} \left(4\varepsilon_s \varepsilon_a \sigma \delta T_a T_a^3 - 4\varepsilon_s \sigma \delta T_s T_s^3 - \rho C_p \frac{\delta T_s}{r_a} + \rho C_p \frac{\delta T_a}{r_a} - \frac{\beta\rho L}{r_a} \left. \frac{\partial q_s^*}{\partial T_s} \right|_{T_s} \delta T_s \right) \\ &\quad - \omega(\delta T_s - \delta T_b) \\ &= \frac{\omega^{1/2}}{P} \left(-4\varepsilon_s \sigma T_s^3 - \frac{\rho C_p}{r_a} - \frac{\beta\rho L}{r_a} \left. \frac{\partial q_s^*}{\partial T_s} \right|_{T_s} - \omega \right) \delta T_s \\ &\quad + \frac{\omega^{1/2}}{P} \rho C_p \frac{\delta T_a}{r_a} + 4 \frac{\omega^{1/2}}{P} \varepsilon_s \varepsilon_a \sigma \delta T_a T_a^3 + \omega \delta T_b \end{aligned} \tag{B.6}$$

After rearrangement of Eq. B.6, where:

$$\tau = \frac{\omega^{1/2}}{P} \frac{\rho C_p}{r_a} t$$

$$r_o = \frac{\rho C_p}{4\varepsilon_s \sigma T_s^3}$$

$$r_g = \frac{\rho C_p}{P\omega^{1/2}}$$

$$\delta_q = \frac{dq_s^*}{dT_s}$$

$$\gamma = \frac{\omega^{1/2} C_p}{L}$$

$$Q' = \frac{\rho C_p}{r_a} \left(4\varepsilon_s \varepsilon_a \sigma T_a^3 \delta T_a + \frac{\omega^{1/2}}{P} \delta T_a + P\omega^{1/2} \delta T_b \right)$$

We get:

$$\frac{d\delta T_s}{d\tau} = - \left(1 + \frac{r_a}{r_o} + \beta \frac{\delta_q}{\gamma} + \frac{r_a}{r_g} \right) \delta T_s + Q' \tag{B.7}$$

Solution to Eq. B.7 is:

$$\delta T_s(\tau) = c_1 e^{-\frac{\tau}{\tau_0}} e^{-\tau} e^{-\beta \frac{\delta_q}{\gamma} \tau} e^{-\frac{\tau}{\tau_g}} + \frac{Q'}{\frac{r_a}{r_g} + 1 + \beta \frac{\delta_q}{\gamma} + \frac{r_a}{r_g}} \tag{B.8}$$

where c_1 is a constant.

B.1. Computation of r_a/r_g

r_a is obtained as aforementioned in the estimation of sensible heat flux.

The LCZ-specific r_g is given by $P\sqrt{\omega}$, where ω is a frequency parameter here at the diurnal scale: $\frac{1}{24 \times 3600} \text{s}^{-1}$ and P is thermal inertia ($\text{J}\cdot\text{m}^{-2}\cdot\text{K}^{-1}\cdot\text{s}^{-1/2}$):

$$P = \sqrt{\frac{Ck}{2}} \tag{C.1}$$

where C is heat capacity ($\text{J}\cdot\text{m}^{-3}\cdot\text{K}^{-1}$) and k is thermal conductivity ($\text{J}\cdot\text{m}^{-1}\cdot\text{s}^{-1}\cdot\text{K}^{-1}$). Here P is defined with a prefactor 2 following that in Bateni et al. (2012), which is different from that without the prefactor 2 in Goward (1981); Oke et al. (2017); Wang et al. (2010). Nevertheless, difference in the

definition of thermal inertia does not change the variation of $\frac{r_a}{r_g}$ the LCZs.

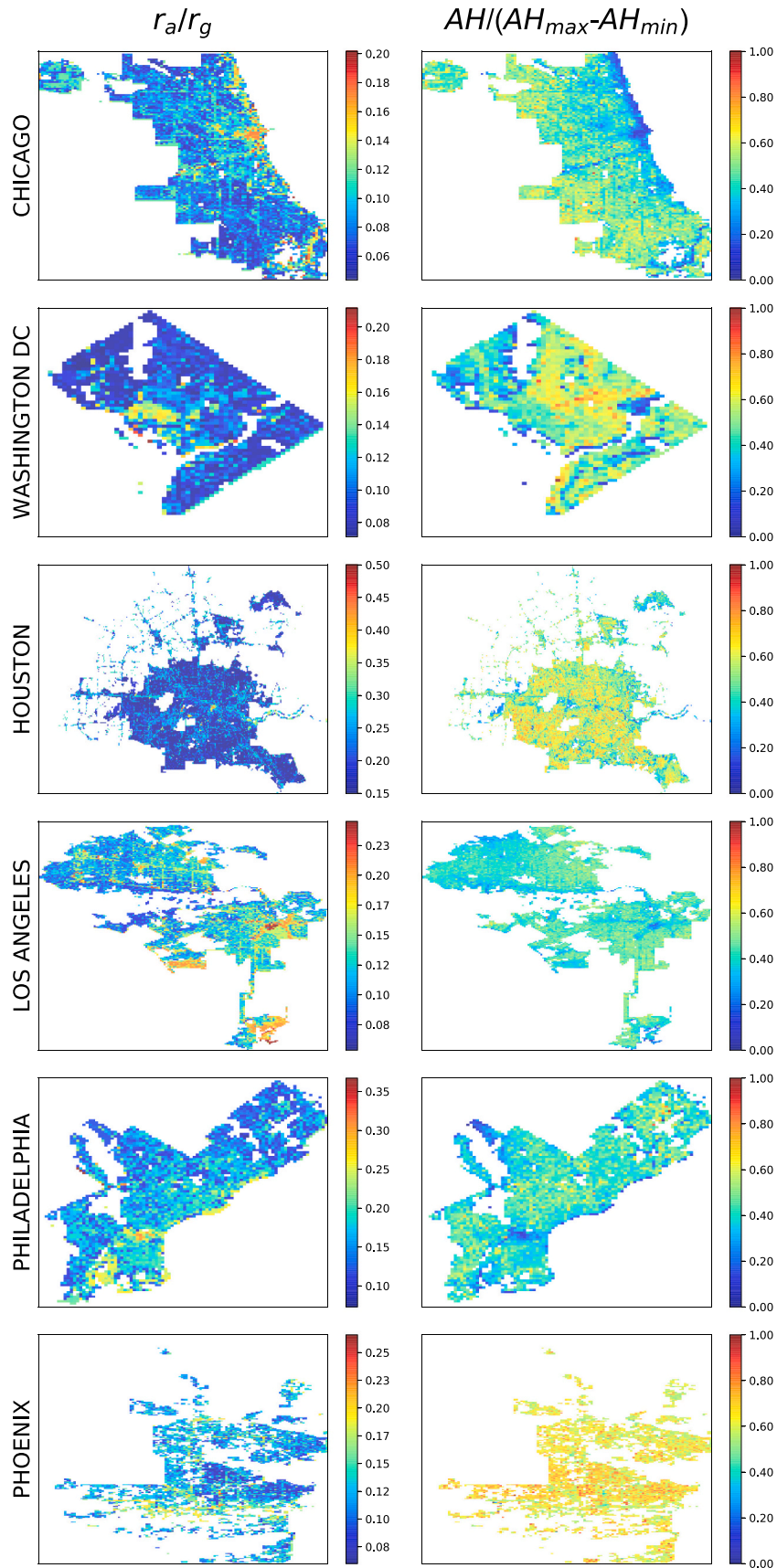


Fig. C.5. Six cities: Energy partitioning efficiencies between sensible and storage heat in contrast with scaled AH.

The retrieval of thermal inertia (P) is based on the heat capacity (C) and thermal conductivity (k) data from LCZ look-up tables. Such thermal properties for three elements (roof, wall and road) constituting urban surfaces are provided across ten LCZ types (Table C.4). In addition, such properties for moist soil (in non built-up area) are from Bateni and Entekhabi (2012). The average water content of clay and sand is assumed to be 0.27, based on which volumetric heat capacity is $2.6 \times 10^6 (Jm^{-3}K^{-1})$ and heat conductivity is $1.35 (Wm^{-1}K^{-1})$. A representative thermal inertia is calculated from a weighted assignment of thermal inertia values of the three major urban compositions. The weight for each LCZ type is decided according to the ratio of surface area between the roof, wall, road and soil (buildings are simplified as cuboids with square basis and four-sided walls). For example, building fraction in LCZ 1 is 50%, which could be approximated to the roof fraction. Consequently, due to the full urbanization in this LCZ class, road surfaces account for the rest of 50%. Meanwhile, the total wall surfaces are ten times that of the roof surface, given average building height is 37.5 m and average building width is 15 m ($\frac{15 \times 37.5 \times 4}{15 \times 15} = 10$). As a result, the ratios among road, roof, wall and soil are 1 : 1 : 10 : 0, based on which those weighted thermal parameters are calculated.

Table C.4

Thermal properties (heat capacity C_i in $Jm^{-3}K^{-1} \times 10^6$ and thermal conductivity k_i in $Jm^{-1}s^{-1}K^{-1}$) and fraction of urban surface type i across LCZs, where i refers to roof, wall, road and soil.

	C_{roof}	C_{wall}	C_{road}	k_{roof}	k_{wall}	k_{road}	roof (%)	wall (%)	road (%)	soil (%)
LCZ 1	1.8	1.8	1.75	1.25	1.09	0.77	8.33	83.33	8.33	0
LCZ 2	1.8	2	1.5	1.25	1.45	0.62	17.19	68.75	12.5	1.56
LCZ 3	1.44	2.05	1.63	1	1.25	0.69	21.24	61.39	13.51	3.86
LCZ 4	1.8	2	1.54	1.25	1.45	0.64	12.45	58.51	14.52	14.52
LCZ 5	1.8	2	1.5	1.25	1.45	0.62	16.30	45.65	21.74	16.30
LCZ 6	1.44	2.05	1.47	1	1.25	0.6	17.24	42.53	20.11	20.11
LCZ 7	2	0.72	1.38	2	0.5	0.51	32.75	56.33	4.37	6.55
LCZ 8	1.8	1.8	1.8	1.25	1.25	0.8	29.41	26.47	33.09	11.03
LCZ 9	1.44	2.56	1.37	1	1	0.55	10.79	28.06	10.79	50.36
LCZ 10	2	1.59	1.49	2	1.33	0.61	17.61	29.58	21.13	31.69

References

- Allen, L., Lindberg, F., Grimmond, C., 2011. Global to city scale urban anthropogenic heat flux: model and variability. *Int. J. Climatol.* 31, 1990–2005.
- Bateni, S., Entekhabi, D., 2012. Relative efficiency of land surface energy balance components. *Water Resour. Res.* 48.
- Bohnstengel, S., Hamilton, I., Davies, M., Belcher, S., 2014. Impact of anthropogenic heat emissions on London's temperatures. *Q. J. R. Meteorol. Soc.* 140, 687–698.
- Brutsaert, W., 1982. *Evaporation into the Atmosphere: Theory, History and Applications*, Volume 1. Springer Science & Business Media.
- Ching, J., Mills, G., Bechtel, B., See, L., Feddema, J., Wang, X., Ren, C., Brousse, O., Martilli, A., Neophytou, M., et al., 2018. Wudapt: an urban weather, climate, and environmental modeling infrastructure for the anthropocene. *Bull. Am. Meteorol. Soc.* 99, 1907–1924.
- Chow, W.T., Salamanca, F., Georgescu, M., Mahalov, A., Milne, J.M., Ruddell, B.L., 2014. A multi-method and multi-scale approach for estimating city-wide anthropogenic heat fluxes. *Atmos. Environ.* 99, 64–76.
- Chrysoulakis, N., Grimmond, S., Feigenwinter, C., Lindberg, F., Gastellu-Etchegorry, J.-P., Marconcini, M., Mitraka, Z., Stagakis, S., Crawford, B., Olofson, F., et al., 2018. Urban energy exchanges monitoring from space. *Sci. Rep.* 8, 1–8.
- Crawford, B., Grimmond, S.B., Gabey, A., Marconcini, M., Ward, H.C., Kent, C.W., 2018. Variability of urban surface temperatures and implications for aerodynamic energy exchange in unstable conditions. *Q. J. R. Meteorol. Soc.* 144, 1719–1741.
- Davenport, A.G., Grimmond, C.S.B., Oke, T.R., Wieringa, J., 2000. Estimating the Roughness of Cities and Sheltered Country, in: *Proceedings 12th Conference on Applied Climatology*. American Meteorological Society, Boston, Asheville NC, pp. 96–99.
- Dong, Y., Varquez, A., Kanda, M., 2017. Global anthropogenic heat flux database with high spatial resolution. *Atmos. Environ.* 150, 276–294.
- Feng, J.-M., Wang, Y.-L., Ma, Z.-G., Liu, Y.-H., 2012. Simulating the regional impacts of urbanization and anthropogenic heat release on climate across China. *J. Clim.* 25, 7187–7203.
- Garratt, J.R., 1994. The atmospheric boundary layer. *Earth Sci. Rev.* 37, 89–134.
- Goward, S.N., 1981. Thermal behavior of urban landscapes and the urban heat island. *Phys. Geogr.* 2, 19–33.
- Grimmond, C., Oke, T.R., 1999. Aerodynamic properties of urban areas derived from analysis of surface form. *J. Appl. Meteorol.* 38, 1262–1292.
- Hanna, S., Marciotto, E., Britter, R., 2011. Urban energy fluxes in built-up downtown areas and variations across the urban area, for use in dispersion models. *J. Appl. Meteorol. Climatol.* 50, 1341–1353.
- Holst, C.C., Tam, C.-Y., Chan, J.C., 2016. Sensitivity of urban rainfall to anthropogenic heat flux: a numerical experiment. *Geophys. Res. Lett.* 43, 2240–2248.
- Hrisiko, J., Ramamurthy, P., Gonzalez, J.E., 2021. Estimating heat storage in urban areas using multispectral satellite data and machine learning. *Remote Sens. Environ.* 252, 112125.
- Iamarino, M., Bevers, S., Grimmond, C., 2012. High-resolution (space, time) anthropogenic heat emissions: London 1970–2025. *Int. J. Climatol.* 32, 1754–1767.
- Johnson, G.T., Oke, T.R., Lyons, T.J., Steyn, D.G., Watson, I.D., Voogt, J.A., 1991. Simulation of surface urban heat islands under 'IDEAL' conditions at night part 1: theory and tests against field data. *Bound.-Layer Meteorol.* 56, 275–294.
- Kanda, M., Kanega, M., Kawai, T., Moriawaki, R., Sugawara, H., 2007. Roughness lengths for momentum and heat derived from outdoor urban scale models. *J. Appl. Meteorol. Climatol.* 46, 1067–1079. <https://doi.org/10.1175/JAM2500.1>
- Kato, S., Yamaguchi, Y., 2005. Analysis of urban heat-island effect using aster and etm+ data: separation of anthropogenic heat discharge and natural heat radiation from sensible heat flux. *Remote Sens. Environ.* 99, 44–54.
- Li, Q., Bou-Zeid, E., Grimmond, S., Zilitinkevich, S., Katul, G., 2020. Revisiting the relation between momentum and scalar roughness lengths of urban surfaces. *Q. J. R. Meteorol. Soc.* 1–31.
- Lindberg, F., Olofson, K., Sun, T., Grimmond, C., Feigenwinter, C., 2020. Urban storage heat flux variability explored using satellite, meteorological and geodata. *Theor. Appl. Climatol.* 1–14.
- Macdonald, R., Griffiths, R., Hall, D., 1998. An improved method for the estimation of surface roughness of obstacle arrays. *Atmos. Environ.* 32, 1857–1864.
- Miao, S., Jiang, W., Wang, X., Guo, W., 2006. Impact assessment of urban meteorology and the atmospheric environment using urban sub-domain planning. *Bound.-Layer Meteorol.* 118, 133–150.
- Moriawaki, R., Kanda, M., Senoo, H., Hagishima, A., Kinouchi, T., 2008. Anthropogenic water vapor emissions in Tokyo. *Water Resour. Res.* 44.
- Nie, W., Zaitchik, B.F., Ni, G., Sun, T., 2017. Impacts of anthropogenic heat on summertime rainfall in Beijing. *J. Hydrometeorol.* 18, 693–712.
- Offerle, B., Grimmond, C.S., Fortuniak, K., 2005. Heat storage and anthropogenic heat flux in relation to the energy balance of a central European city Centre. *Int. J. Climatol.* 25, 1405–1419.
- Oke, G., Johnson, T., Steyn, D.G., Watson, I.D., 1991. Simulation of surface urban heat islands under 'ideal' conditions at night part 2: diagnosis of causation. *Bound.-Layer Meteorol.* 56, 339–358.
- Oke, T., Mills, G., Christen, A., Voogt, J.A., 2017. *Urban climates*. Cambridge University Press.
- Pigeon, G., Legain, D., Durand, P., Masson, V., 2007. Anthropogenic heat release in an old European agglomeration (Toulouse, France). *Int. J. Climatol.* 27, 1969–1981.
- Quah, A.K., Roth, M., 2012. Diurnal and weekly variation of anthropogenic heat emissions in a tropical city, Singapore. *Atmos. Environ.* 46, 92–103.
- Roberts, S.M., Oke, T.R., Grimmond, C., Voogt, J.A., 2006. Comparison of four methods to estimate urban heat storage. *J. Appl. Meteorol. Climatol.* 45, 1766–1781.
- Sailor, D.J., 2011. A review of methods for estimating anthropogenic heat and moisture emissions in the urban environment. *Int. J. Climatol.* 31, 189–199.
- Sailor, D.J., Lu, L., 2004. A top-down methodology for developing diurnal and seasonal anthropogenic heating profiles for urban areas. *Atmos. Environ.* 38, 2737–2748.
- Stewart, I.D., Oke, T.R., 2012. Local climate zones for urban temperature studies. *Bull. Am. Meteorol. Soc.* 93, 1879–1900.
- Sun, T., Wang, Z.-H., Ni, G.-H., 2013. Revisiting the hysteresis effect in surface energy budgets. *Geophys. Res. Lett.* 40, 1741–1747.

- Sun, T., Wang, Z.H., Oechel, W.C., Grimmond, S., 2017. The analytical objective hysteresis model (AnOHM v1.0): methodology to determine bulk storage heat flux coefficients. *Geosci. Model Dev.* 10, 2875–2890.
- Swaid, H., 1995. Urban climate related aspects of the force-restore method. *Atmos. Environ.* 29, 3401–3409.
- Wang, J., Bras, R., Sivandran, G., Knox, R., 2010. A simple method for the estimation of thermal inertia. *Geophys. Res. Lett.* 37.
- Wang, Z.-H., Bou-Zeid, E., Smith, J.A., 2011. A spatially-analytical scheme for surface temperatures and conductive heat fluxes in urban canopy models. *Bound.-Layer Meteorol.* 138, 171–193.
- Wieringa, J., 1986. Roughness-dependent geographical interpolation of surface wind speed averages. *Q. J. R. Meteorol. Soc.* 112, 867–889.
- Wong, M.S., Yang, J., Nichol, J., Weng, Q., Menenti, M., Chan, P.W., 2015. Modeling of anthropogenic heat flux using hj-1b chinese small satellite image: a study of heterogeneous urbanized areas in Hong Kong. *IEEE Geosci. Remote Sens. Lett.* 12, 1466–1470.
- Yang, J., Wang, Z.-H., 2014. Land surface energy partitioning revisited: a novel approach based on single depth soil measurement. *Geophys. Res. Lett.* 41, 8348–8358.
- Zhang, L., Brook, J.R., Vet, R., 2003. A revised parameterization for gaseous dry deposition in air-quality models. *Atmos. Chem. Phys.* 3, 2067–2082.
- Zhang, W., Villarini, G., Vecchi, G.A., Smith, J.A., 2018. Urbanization exacerbated the rainfall and flooding caused by hurricane Harvey in Houston. *Nature* 563, 384–388.
- Zhang, P., Yuan, C., Sun, Q., Liu, A., You, S., Li, X., Zhang, Y., Jiao, X., Sun, D., Sun, M., et al., 2019. Satellite-based detection and characterization of industrial heat sources in China. *Environ. Sci. Technol.* 53, 11031–11042.
- Zhou, Y., Weng, Q., Gurney, K.R., Shuai, Y., Hu, X., 2012. Estimation of the relationship between remotely sensed anthropogenic heat discharge and building energy use. *ISPRS J. Photogramm. Remote Sens.* 67, 65–72.